


Research Article

Mechanical Characteristics and Mesostructural Damage of Saturated Limestone under Different Load and Unload Paths

Jielin Li,^{1,2} Liu Hong ,¹ Keping Zhou,¹ Caichu Xia ,^{2,3} and Longyin Zhu^{1,2,4}

¹School of Resources and Safety Engineering, Central South University, Changsha 410083, China

²Key Laboratory of Rock Mechanics and Geohazards of Zhejiang Province, Shaoxing 312000, China

³College of Civil Engineering, Tongji University, Shanghai 200092, China

⁴Northern Engineering & Technology Corporation, MCC, Dalian 116000, China

Correspondence should be addressed to Liu Hong; mining-hongliu@csu.edu.cn and Caichu Xia; xiacaichu@tongji.edu.cn

Received 12 May 2020; Revised 22 October 2020; Accepted 1 December 2020; Published 15 January 2021

Academic Editor: Zhongguo John Ma

Copyright © 2021 Jielin Li et al. This is an open access article distributed under the Creative Commons Attribution License, which permits unrestricted use, distribution, and reproduction in any medium, provided the original work is properly cited.

To study the evolutionary characteristics of mesostructural damage to saturated limestone under different loading and unloading paths, three types of loading and unloading tests involving three different loading rates and initial peak stresses were performed. Nuclear magnetic resonance technology and scanning electron microscopy were used to investigate the evolutionary characteristics of pore water during the loading and unloading of the limestone. The results indicated that, with an increase in the initial peak stress, the rock viscoplasticity gradually decreased, and the variation of pore radius and the reduction of bound water decreased. With an increasing loading rate, the mesostructure evolution law under disturbance-increasing amplitude (DIA) cycling was opposite to those under increasing amplitude (IA) and repeated-increasing amplitude (RIA) cycling. With the increasing loading stress level, the porosity decreased and then increased. Under increasing amplitude cycling, a larger initial porosity resulted in higher pore compaction and expansion limits. Reducing the initial peak stress inhibited the pore expansion, whereas it had the opposite effect under RIA and DIA cycling. During loading and unloading, bound water exists in pores of organic matter and mesopores, and free water exists in macropores of intergranular and transgranular fractures. These changes indicate certain laws under different loading and unloading paths. The results of this study indicate that the mesostructure characteristics of rock depend on the loading and unloading paths.

1. Introduction

Deep mining is an inevitable trend for the future mining of mineral resources. Under the complex geological conditions and stressful environments of deep mining, a large amount of elastic energy is stored inside the rocks, resulting in diverse mechanics under complex loads and moisture conditions. Mesostructure and shallow ore rocks differ significantly with regard to their physical properties, deformation, and fracture behavior. Therefore, studying the damage to the rock and degradation of the rock mechanical properties under loading and unloading is crucial for the stability analysis of deep rock masses.

Different mining environments cause different loading and unloading formations in underground rock bodies, and the physical and mechanical properties of rocks under

different loading and unloading methods differ significantly. A higher loading rate results in a more ductile response in the stress-strain curve [1], weaker rock viscoplasticity, more brittle fracture, a higher peak strength and peak strain, faster strength degradation, and a shorter compaction stage and plastic stage [2]. A higher loading stress results in a higher probability of the overall deformation of rocks developing toward brittleness, earlier failure, a higher peak strength [3], a lower elastic modulus, and a longer compaction stage and plastic stage. Therefore, it is important to study the physical and mechanical characteristics of rocks under different loading and unloading paths to analyze the mechanical response of deep rock masses.

The mesostructural damage of rocks is time varying; in the microscopic evolution during loading and unloading, the damage changes from the number of micropores increasing

gradually to micropore expansion and penetration, followed by macropore expansion. The permeability boundary broadens outward through channels formed between microcracks, resulting in crystal fractures that lead to breaks [4]. During loading and unloading, the porosity and mesodamage of rocks increase, first slowly and then rapidly. Thus, it is crucial to study the evolution of the parameters, such as the porosity during loading and unloading, to evaluate the deterioration of the mesostructure and predict the development of mesostructural damage.

The mesostructural damage characteristics of rocks are significantly affected by their mechanical environment; furthermore, the characteristics differ depending on the loading and unloading rates and loading stresses [5]. Increasing the loading rate transforms the fragmentation from parse to dramatic pulverization. When the initial stress is higher, the expansion of rock pores is more stable, the penetration behavior of large fractures is more prominent, and the porosity is higher at the time of rock failure. Reducing the initial stress weakens the promotion effect of the load on the lateral strain and microcrack expansion [6].

Additionally, the mesostructure and damage of rocks directly affect their macroscopic physical and mechanical properties. The elastic modulus of rocks increased with the quartz content, grain size, compaction, and density, and the rock strength was affected by the feldspar content [7]. A larger amount of water in rocks resulted in a larger softening coefficient and higher viscoplasticity [8], leading to more significant plastic deformation during loading, a lower residual stress, and a smaller amount of stress energy released during failure. According to the foregoing findings, various mesoparameters affect the mechanical properties of underground rock masses. Consequently, the laboratory test conditions differ from those of underground rock masses with regard to the actual force. The results obtained from simple constant-amplitude loading and unloading tests are not sufficient for guiding the construction of deep rock masses.

To examine the effects of different loading and unloading paths on the mechanical characteristics and mesostructural damage of saturated rocks, three types of loading and unloading tests were performed, along with mesostructure testing with different loading rates and initial cyclic peak stress controls. Subsequently, the mechanical properties and mesostructure characteristics of rocks under different loading and unloading paths were analyzed.

2. Materials and Methods

2.1. Rock Samples. Gaofeng tin mine in Guangxi, China, was taken as the research background of this study, in which the deep surrounding rock is mainly limestone; therefore, limestone with a massive structure obtained from the Gaofeng tin mine was taken as the rock sample. X-ray fluorescence (XRF) and X-ray diffraction (XRD) spectroscopy results (see Tables 1 and 2) for the rock samples indicated that the rock was composed of mud crystal grains that were filled with calcite and cemented with serpentinite, dolomite, pyrite, and a small amount of talc. According to

TABLE 1: Mineral elements in the limestone according to XRF.

Element	Ca	S	Zn	Fe	Si	Mg
Content/(%)	60.194	2.704	0.274	0.818	0.222	0.212

the ISRM method for rock mechanics laboratory tests [9], the limestone was processed into cylindrical samples with dimensions of 100 mm × 50 mm, and the samples were vacuum saturated after they were grouped. The average porosity of the rock samples measured via nuclear magnetic resonance (NMR) was 0.53%.

Tables 1 and 2 are reproduced from the work of Li et al. [10] (under the Creative Commons Attribution License/public domain).

Uniaxial compression pretests at loading rates of 0.15, 0.2, and 0.3 mm/min were performed on partial rock samples to obtain the basic mechanical parameters of limestone with different loading rates, as shown in Table 3, and the average compressive strength of 25.03 MPa can be obtained via the calculation.

2.2. Experimental Procedure. According to the amplitude of each cyclic peak stress, the loading and unloading methods can generally be categorized into constant-amplitude, increase-amplitude, decrease-amplitude, and delayed-amplitude loading and unloading. According to the theory of ground pressure and strata control, the bearing pressure of the underground surrounding rock and pillar is redistributed by mining. From the goaf to the deep surrounding rock, a low-stress area, high-stress area, and constant-stress area are formed successively [11]. The bearing stress in the low-stress area is lower than the original rock stress, and its variation range gradually increases with the expansion of the goaf [12]. The bearing stress in the high-stress area is a stress concentration formed induced by the repeated excavation process [13], and the bearing stress in the constant-stress area tends to be steady, with only small changes [14]. According to bearing stress distribution area, three types of loading and unloading methods were used:

- (1) Increasing amplitude (IA) cycling: the peak stress is increased in steps of $\sigma_+ = 5$ MPa
- (2) Repeated-increasing amplitude (RIA) cycling: loading and unloading are performed repeatedly under a constant peak stress, followed by loading and unloading under the peak stress after an increase of $\sigma_+ = 7.5$ MPa
- (3) Disturbance-increasing amplitude (DIA) cycling: after loading to the peak stress σ , multiple disturbance loading and unloading cycles with a magnitude of $1/5\sigma$ are applied, and the loading and unloading are then continued under the peak stress after an increase of $\sigma_+ = 7.5$ MPa

The schematics of the three types of loading and unloading methods' path are shown in Figure 1.

According to the three aforementioned types of loading and unloading methods, to study the effects of different

TABLE 2: Mineral composition of the limestone.

Mineral	Calcite, dolomite compounds	Serpentinite	Pyrite	Talc	Zinc sulfide	Quartz
Content/(%)	94.4	1.4	2.2	1.0	0.8	0.2

TABLE 3: Basic parameters of rock samples.

Loading rate v /(mm/min)	Compressive strength (σ_c /MPa)	Elastic modulus (E_c /GPa)	Maximum plastic strain for the whole test (ϵ_{max})	Residual stress (σ_r /MPa)
0.15	26.36	3.97	0.00491	15.22
0.2	24.81	3.15	0.01548	9.87
0.3	23.94	1.58	0.02040	6.19
Average value	25.03	2.90	0.01360	10.43

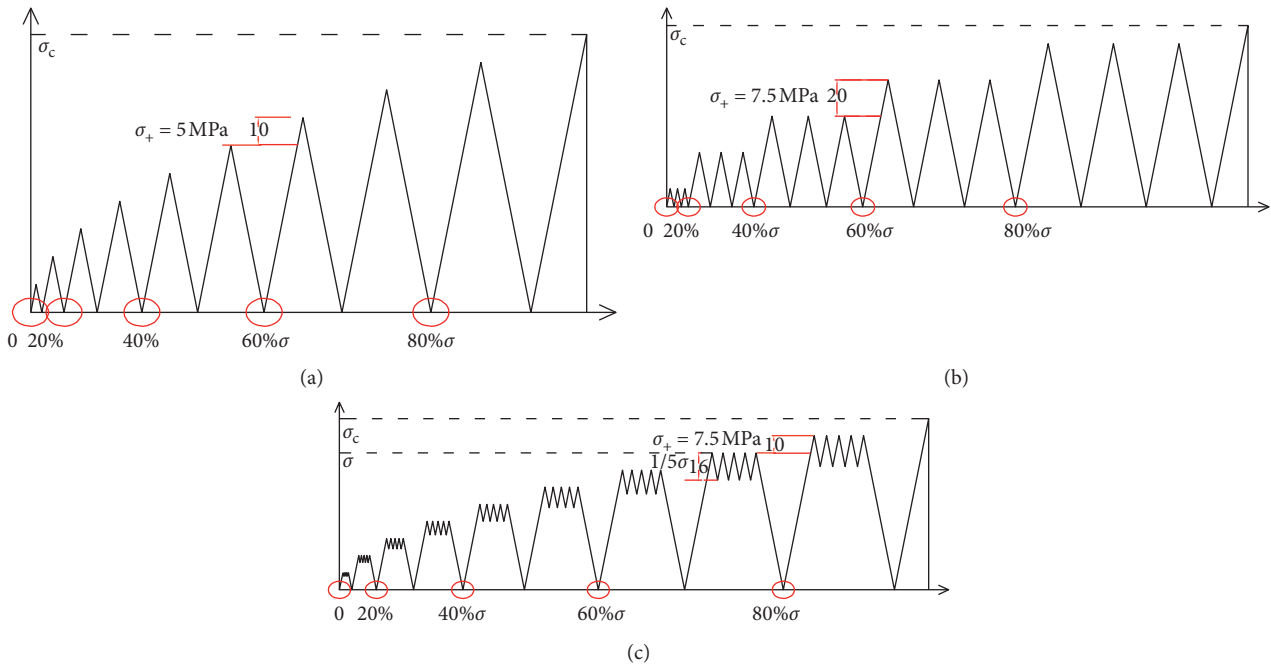


FIGURE 1: Three loading and unloading methods: (a) IA cycling; (b) RIA cycling; and (c) DIA cycling.

loading rates (v) on the mesostructural damage of rocks, three loading rates were used: 0.15, 0.2, and 0.3 mm/min [15]. To compare and analyze the mesostructure characteristics of rocks under initial cyclic peak stresses (σ_0) of 10%, 30%, and 50% of σ_c (where $\sigma_c = 25.03$ MPa represents the average compressive strength of limestone), three initial peak stresses were used: 2.5, 7.5, and 12.5 MPa, respectively. The 15 loading and unloading paths generated are presented in Table 4. In each loading and unloading test, the displacement control method was adopted, and the unloading rate was fixed at 1 mm/min.

For each loading and unloading condition, three rock samples were selected for testing; i.e., a total of 45 tests were performed. Furthermore, 0%, 20%, 40%, 60%, and 80% of σ_c were set as the NMR test nodes during the loading and unloading, and the porosity and NMR T_2 spectrum data of the rock samples were obtained. In the test, if the rock sample did not reach the peak stress set in the cycle and unload itself, unloading to zero stress was performed manually, and the original loading scheme was applied.

TABLE 4: Loading and unloading scheme.

Rate and initial peak stress control	Loading and unloading methods		
	IA cycling	RIA cycling	DIA cycling
$v = 0.15$ mm/min, $\sigma_0 = 2.5$ MPa	(1)	(6)	(11)
$v = 0.2$ mm/min, $\sigma_0 = 2.5$ MPa	(2)	(7)	(12)
$v = 0.3$ mm/min, $\sigma_0 = 2.5$ MPa	(3)	(8)	(13)
$v = 0.2$ mm/min, $\sigma_0 = 7.5$ MPa	(4)	(9)	(14)
$v = 0.2$ mm/min, $\sigma_0 = 12.5$ MPa	(5)	(10)	(15)

After loading to failure, the damage appearance of the rock was recorded, and a scanning electron microscope (SEM) was used to investigate the mechanical deformation and porosity and obtain T_2 spectra and electron microscope scanning results for the entire loading and unloading processes.

The test equipment and process are shown in Figure 2.

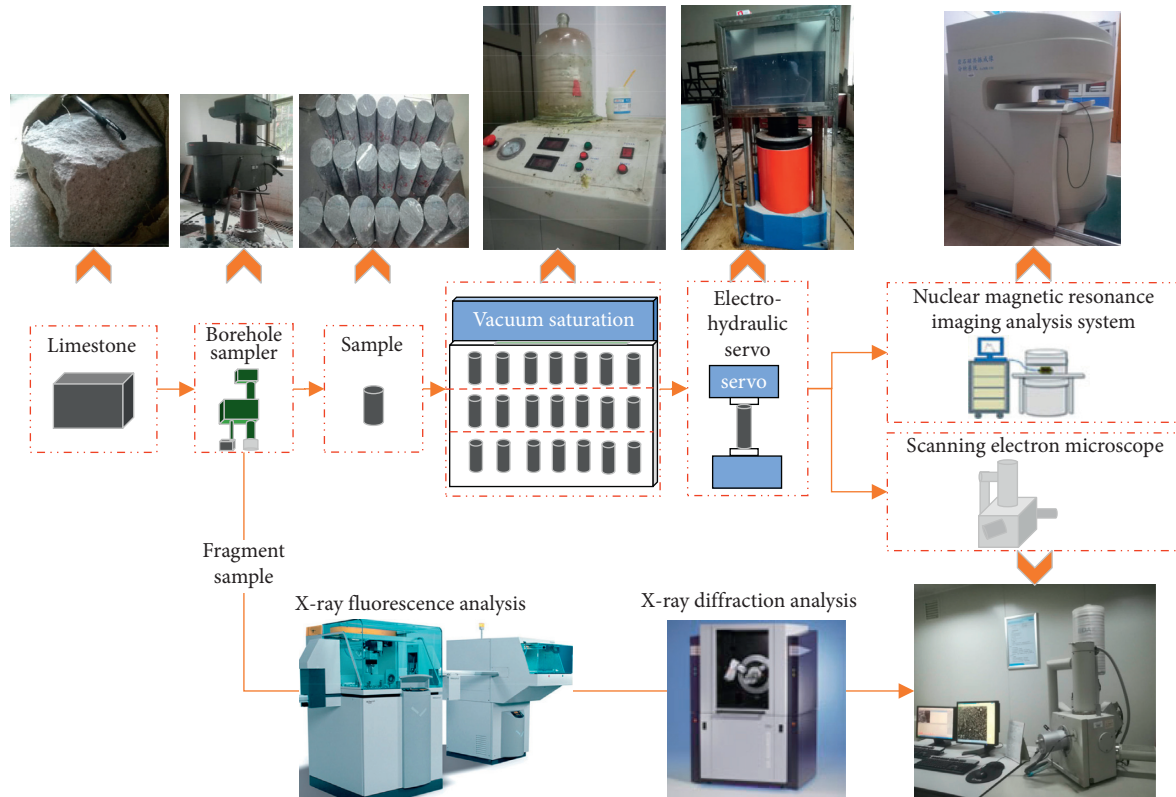


FIGURE 2: Experimental instrument flowchart.

3. Analysis of Mechanical Characteristics under Three Loading and Unloading Methods

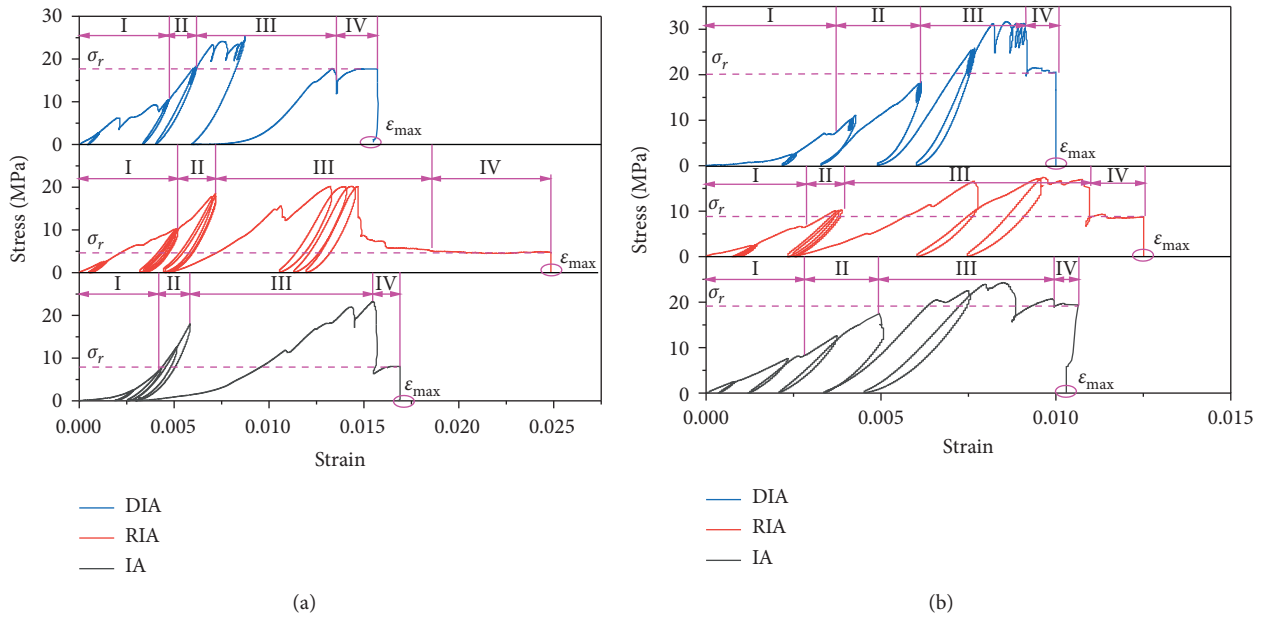
3.1. Mechanical Characteristics under Different Loading Rates and Initial Peak Stresses. The typical test results of the rock samples under each loading and unloading path were analyzed, and the changes in the rock physical and mechanical properties at different loading rates (v) and initial peak stresses (σ_0) under the three loading and unloading methods are presented in Table 5. When the rock underwent failure, it released all the plastic energy; thus, to analyze the whole deformation of the rock, the strain at failure was taken as the maximum plastic strain for the whole test, ε_{\max} . Under the IA and RIA cycling, with an increase in the loading rate, the plastic strain ε_{\max} of the rock increased gradually, and the residual stress σ_r decreased. For all the loading and unloading methods, as the initial peak stress increased, the plastic strain of the rock gradually decreased loading and unloading, and the residual stress and strength σ_c gradually increased. Additionally, at different loading rates, the change laws of the strength and plastic strain of the rocks under the RIA and DIA cycling were identical, whereas they were opposite under the other loading and unloading conditions. This indicates that, during the RIA and DIA cycling, under the influence of the loading rate, the rock primarily maintained its integrity through plastic deformation and, hence, resisted external forces, resulting in the peak strength; however, the strength of the rock under the other loading conditions depended primarily on its brittleness.

3.2. Mechanical Characteristics under Different Loading and Unloading Methods. Figure 3 presents the stress-strain curves of rocks under different loading and unloading methods. As shown, for the RIA and IA, the curves fluctuated in the loading stage of the plastic stage. The duration of the plastic stage under the different loading and unloading methods decreased in the following order: RIA > IA > DIA; the plastic strain ε_{\max} decreased in this order. While the residual stress σ_r and strength increased in this order, both of them exhibit behaviors opposite to that of the plastic strain, and the maximum plastic strain before the plastic stage becomes smaller in the abovementioned order. According to the analysis, the difference in the plastic strain of the rock generated under different loading and unloading methods primarily occurs in the plastic stage; therefore, the laws governing the duration relationship in the plastic stage and the relationship of the plastic strain are consistent. Furthermore, according to the relationship between the durations of the plastic stage, it is clear that the rock durability against external forces in the plastic stage is directly proportional to the amount of time consumed for a complete loading and unloading cycle.

Rocks under RIA cycling are subjected to multiple complete cycles of the constant peak stress after each loading section, and the loading stress of multiple cycle is identical with that of the loading section; therefore, the rocks could resist external forces for a long time, and the pores in each loading section that did not expand to the limit underwent a secondary expansion in the later constant peak stress cycle,

TABLE 5: Evolution laws of the mechanical properties under different loading rates and initial peak stresses.

		Continuity of the loading curve in the plastic stage and previous cycle	Concave tendency of the curve before the plastic stage	Initial tangent modulus of each cycle	ϵ_{\max}	σ_r	σ_c	Remark	
As the loading rate ν increases	IA	Worse	More obvious	Smaller	Larger	Lower	Lower	Earlier large perturbation formation	
	RIA	Better	More obvious	Smaller	Larger	Lower	Higher		
	DIA	Worse	Less obvious	Larger	Smaller	Higher	Lower		
As the initial peak stress σ_0 increases	IA	Better	Less obvious	Larger	Smaller	Higher	Higher	Earlier decrease of load curve tangent modulus	
	RIA	Better	More obvious	Smaller	Smaller	Higher	Higher		
		DIA	Better	Less obvious	Larger	Smaller	Higher	Higher	Less strain between adjacent cycles

FIGURE 3: Experimental instrument flowchart. Stress-strain curves of the rock for different loading and unloading methods: (a) $\nu = 0.2$ mm/min, $\sigma_0 = 2.5$ MPa; (b) $\nu = 0.15$ mm/min, $\sigma_0 = 2.5$ MPa. I, compression stage; II, linear-elastic stage; III, plastic stage; and IV, softening stage.

resulting in a larger deformation and longer deformation time of the rocks in the plastic stage and a lower rock strength. In the DIA cycling, the multiple disturbance cycles fatigued the rock; therefore, this method had the shortest loading process, resulting in the shortest plastic stage and the highest strength.

As shown in Figure 3, the duration of the softening stage decreased in the following order: RIA > DIA > IA. Additionally, the curves for RIA and DIA cycling exhibited large strains and long-term fluctuations between cycles, with peak stresses of 2.5 and 10 MPa, respectively. The duration at the softening stage indicates that the softening behavior after rock failure was related to the fluctuation in the loading curve of the compaction stage and that the longest softening stage of RIA cycling is the only method for applying a complete loading and unloading cycle in the later part of the plastic stage. Thus, the highest residual resistance of the rock was observed under RIA cycling, which resulted in a low residual stress σ_r in the softening stage.

4. Analysis of Pore Evolution Characteristics under Three Loading and Unloading Methods

NMR technology has been widely used in the study of the mesostructural damage of rocks because it is fast, efficient, and nondestructive and yields accurate and sensitive data, as well as intuitive and rich results. According to the principle of NMR, when the nuclear magnetic resonance machine sends out the radio frequency pulse, the hydrogen proton in the detection object will be excited, and for the saturated rock, hydrogen proton only exists in the liquid. When the radio frequency pulse is terminated, the excited hydrogen proton will gradually release the absorbed energy and return to the state before excitation. This process is called relaxation, and the duration required to complete this process is called relaxation time.

The relaxation mechanisms generally include fluid free relaxation, surface relaxation, and molecular self-diffusion

relaxation. Fluid free relaxation is the inherent relaxation characteristic of liquid, which is generally determined by liquid viscosity, chemical composition, external temperature, and pressure. Surface relaxation occurs on the solid-liquid contact surface (in this test, it occurs on the particle surface of rock), and surface relaxation changes with the lithology. Molecular self-diffusion relaxation is a special relaxation characteristic of fluid in the gradient magnetic field. Because the abovementioned three functions exist at the same time, the crosswise relaxation rate $1/T_2$ is given as follows [16]:

$$\frac{1}{T_2} = \frac{1}{T_{2\text{free}}} + \rho_2 \left(\frac{S}{V} \right)_{\text{pore}} + \frac{D(\gamma G T_E)^2}{12}, \quad (1)$$

where T_2 represents the crosswise relaxation time (in ms); $T_{2\text{free}}$ represents the fluid free relaxation time (in ms); S represents the surface area of pores (in cm^2); V represents the volume of pores (in cm^3), $(S/V)_{\text{pore}}$ represents the specific surface area of pores (in cm^{-1}); ρ_2 represents the crosswise surface relaxation strength (in $\mu\text{m}/\text{ms}$), which varies according to the rock type; D represents the diffusion coefficient; γ represents the gyromagnetic ratio (in $\text{rad}/(\text{S}\cdot\text{T})$); G represents the magnetic gradient (in Gs/cm); and T_E represents the echo time (in ms).

If there is only one pure fluid in the pore, the fluid free relaxation time is significantly lower than the surface relaxation time; thus, $T_{2\text{free}}$ can be ignored. If the magnetic field is uniform (i.e., the magnetic gradient G is small) and T_E is short, the diffusion relaxation can also be ignored. Therefore, T_2 and ρ_2 satisfy the following relationship [17], [18]:

$$\frac{1}{T_2} = \rho_2 \left(\frac{S}{V} \right)_{\text{pore}}. \quad (2)$$

As indicated by equation (2), the crosswise relaxation rate $1/T_2$ of the rocks is positively correlated to the specific surface area of pores.

For the pores of the sample can be simplified as spherical or columnar, the throat radius is related to the pore radius. Thus, equation (2) can be transformed into the relationship between the T_2 relaxation time and the pore radius as follows:

$$\frac{1}{T_2} = \frac{\rho_2}{r} F_s, \quad (3)$$

where r represents the pore radius and F_s is a geometric factor.

Equation (2) can be further transformed as follows:

$$r = C T_2. \quad (4)$$

Rocks with different physical properties have different C values. We refer to the relationship between the pore radius of dense limestone and T_2 [19], using $C = 0.01 \mu\text{m}/\text{ms}$. Therefore, equation (3) can be expressed as

$$r = 0.01 T_2. \quad (5)$$

Owing to the complexity of the pore structure and the permeability of limestone, a fixed pore-radius division

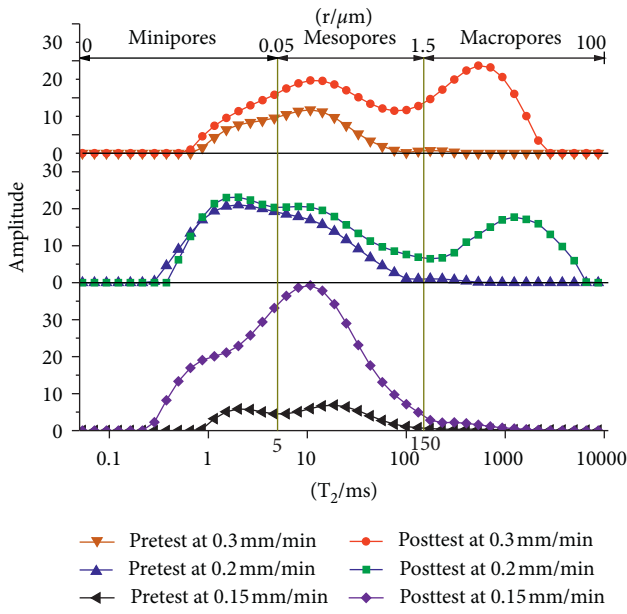
method does not exist. Scholars have categorized the pore radius into three ranges: minipores ($r \leq 0.002 \mu\text{m}$), mesopores ($0.002 \mu\text{m} \leq r \leq 0.05 \mu\text{m}$), and macropores ($0.05 \mu\text{m} \leq r$) for dense limestone [20], as well as minipores ($r \leq 0.5 \mu\text{m}$), mesopores ($0.5 \mu\text{m} \leq r \leq 1.5 \mu\text{m}$), and macropores ($1.5 \mu\text{m} \leq r$) for complex carbonate [21]. According to the T_2 spectrum distribution of pretest and posttest rocks under different loading and unloading conditions (shown in Figure 4), combined with the division method of previous scholars, the authors categorized the pores into three types: minipores ($r \leq 0.05 \mu\text{m}$), mesopores ($0.05 \mu\text{m} \leq r \leq 1.5 \mu\text{m}$), and macropores ($1.5 \mu\text{m} \leq r$). Subsequently, using equation (4), the 0–5, 5–150, and >150 ms ranges of the T_2 distribution were categorized as minipores, mesopores, and macropores, respectively.

4.1. NMR T_2 Spectrum Distributions under Different Loading Rates and Initial Peak Stresses. As shown in equation (4), the T_2 was directly proportional to the pore radius. Therefore, the amplitude of the T_2 spectrum was positively correlated to the number of pores with a certain radius, and the T_2 spectrum distribution agreed with the pore-radius distribution of the rock sample [16].

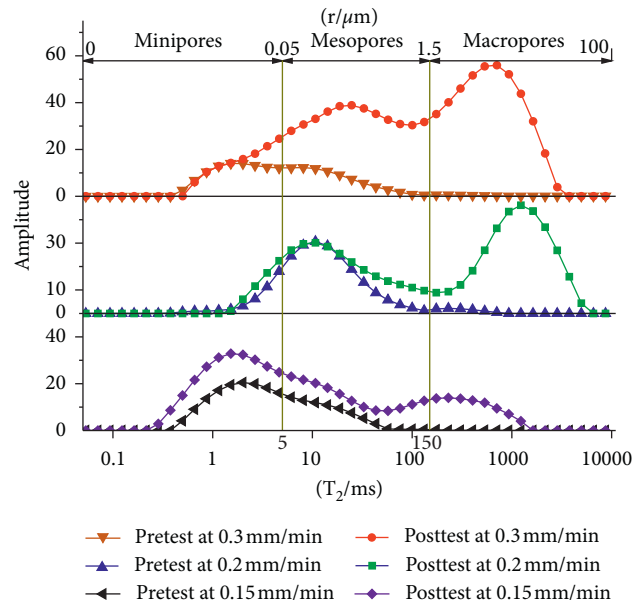
As shown in Figure 4, the T_2 distribution of limestone primarily exhibits 2–3 peaks, and the pretest relaxation time T_2 is distributed within 1–100 ms. The range of T_2 after the test is extended to 1–5000 ms, and the rightmost T_2 spectrum peak is formed; i.e., macropores are generated.

As shown in Figure 4(a), under IA cycling, compared with the cases of $\nu = 0.15$ and $0.2 \text{ mm}/\text{min}$, the posttest peaks of the minipores were smaller under $\nu = 0.3 \text{ mm}/\text{min}$, and the pore-radius distribution was more continuous between the peaks of minipores and mesopores. This is because at a higher loading rate, the minipores were more likely to undergo irrecoverable plastic deformation [22], which promoted their expansion into mesopores, resulting in a more uniform distribution. As shown in Figure 4(d), a higher initial peak stress resulted in a smaller pore change for each pore radius of the mesopores, as well as less obvious spectral peaks of the mesopores after the test. Compared with the case of $\nu = 0.2 \text{ mm}/\text{min}$, the spectral peaks of the minipores were larger for $\nu = 0.3 \text{ mm}/\text{min}$. According to the analysis, increasing the initial peak stress increased the compaction deformation of the pores [23], making it difficult for some minipores to continue expanding, which resulted in the large peak of the minipores and the invisible peak of the mesopores.

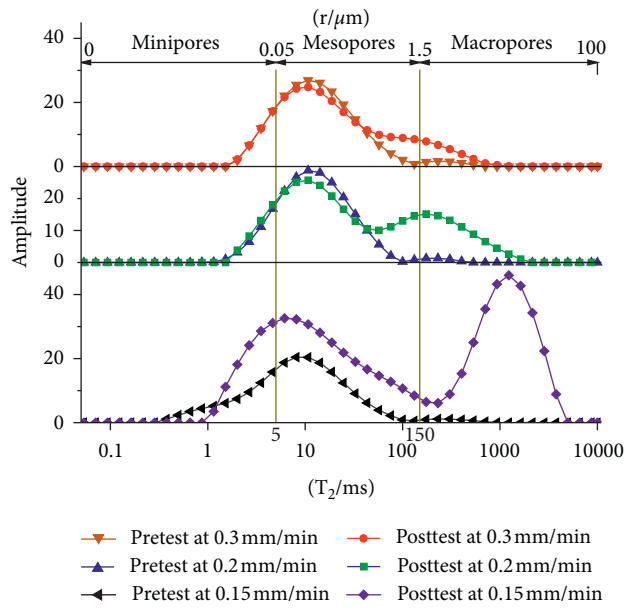
As shown in Figure 4(b), under RIA cycling, with an increase in the loading rate, the increase in minipores between the pretest and posttest samples gradually decreased. For macropores, the increase was larger, and the rightward shift of the T_2 spectrum was more obvious. After the test, the spectrum peak of the minipores gradually disappeared. The analysis indicates that increasing the loading rate promoted the conversion of minipores to macropores. Consequently, the size ranges of the mesopores and macropores increased, resulting in a larger rightward shift of the T_2 spectrum. Furthermore, at $\nu = 0.3 \text{ mm}/\text{min}$, the curve of small pores in



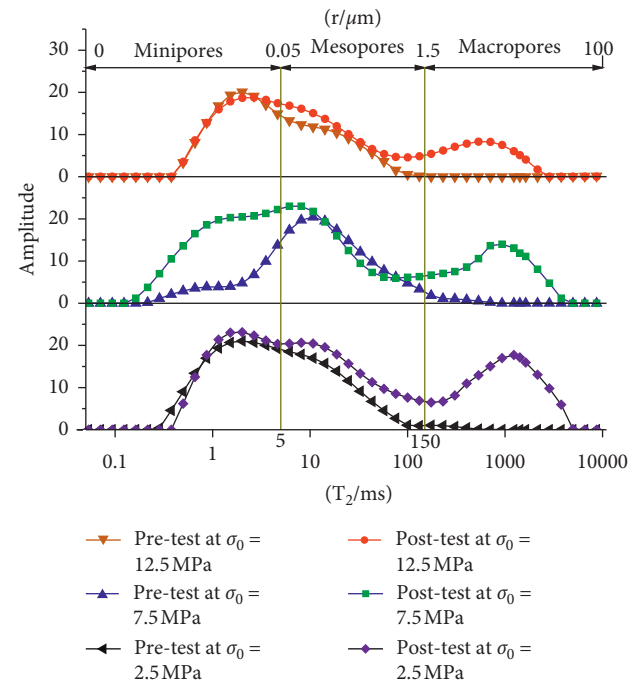
(a)



(b)



(c)



(d)

FIGURE 4: Continued.

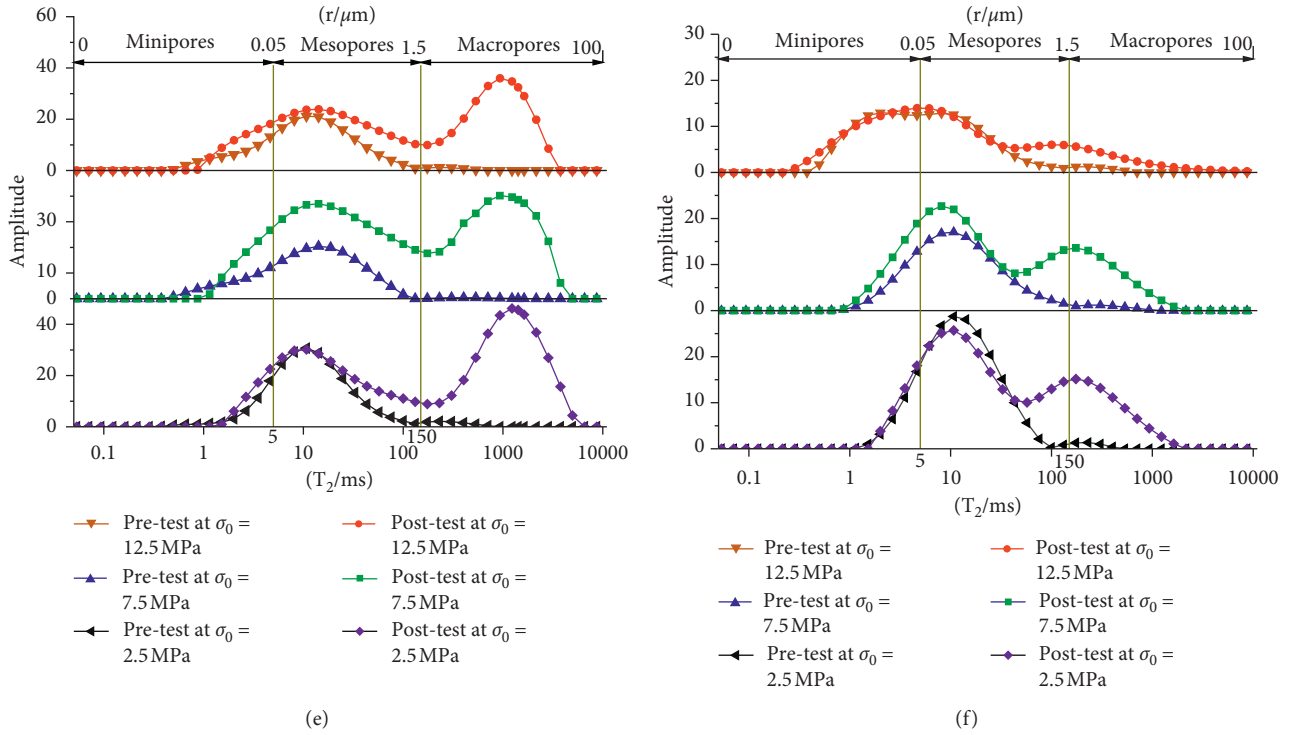


FIGURE 4: T_2 spectrum distributions for different loading rates and initial peak stresses before and after the test: (a) $\sigma_0 = 2.5$ MPa, IA cycling; (b) $\sigma_0 = 2.5$ MPa, RIA cycling; (c) $\sigma_0 = 2.5$ MPa, DIA cycling; (d) $\nu = 0.2$ mm/min, IA cycling; (e) $\nu = 0.2$ mm/min, RIA cycling; and (f) $\nu = 0.2$ mm/min, DIA cycling.

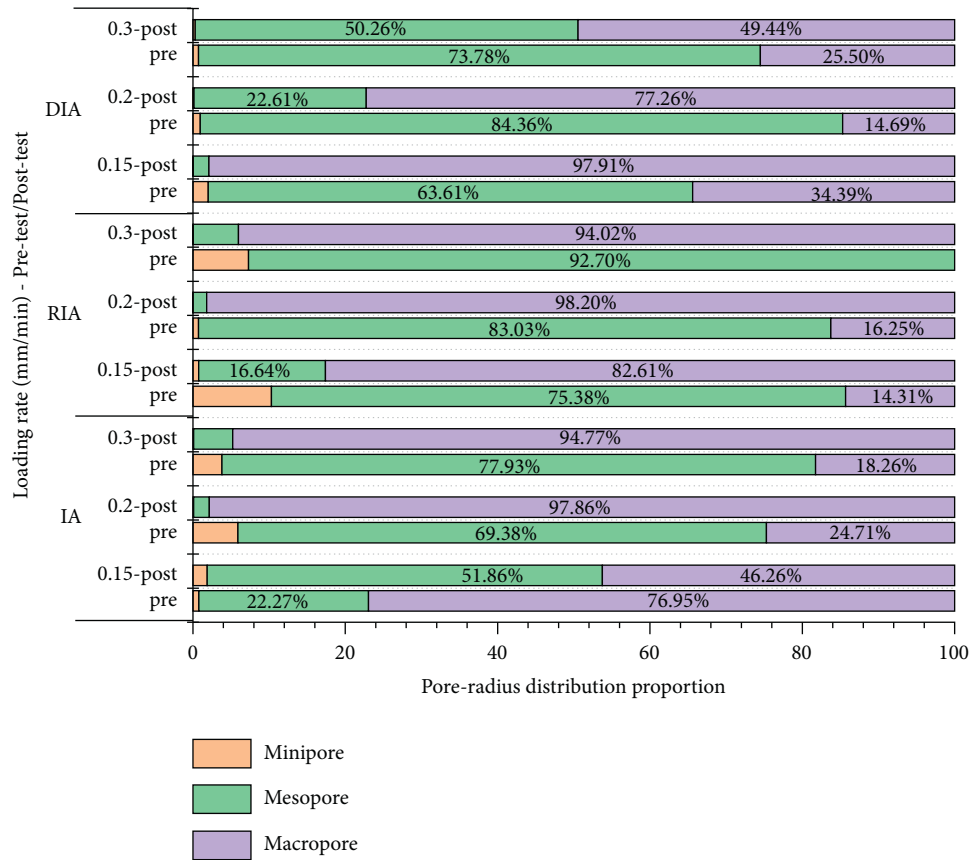
the mesopores range transformed from unchanged before the test to a significant increase after the test. According to the analysis, at high loading rates, the large-scale growth of macropores inhibited the expansion of the mesopores due to the pore-water pressure [24], which increased the accumulation of small pores in the mesopore range. As shown in Figure 4(e), the increase in the initial peak stress reduced the increase in the macropores. This is because under the high initial peak stress of RIA cycling, multiple large loads were applied, causing a permanent deformation of the pores [25] and, thus, a small increase in macropores.

As shown in Figure 4(c), with an increase in the loading rate, the difference between the pre- and posttest T_2 spectra amplitude decreased. There was a reduction in pores at all the loading rates. The reduction in minipores occurred at $\nu = 0.15$ mm/min, but the reduction in mesopores occurred at $\nu = 0.2$ and 0.3 mm/min, indicating that increasing the loading rate suppressed the expansion of large pores. Moreover, with the increasing loading rate, the rightward shift of the T_2 spectrum between pretest and posttest samples became less obvious, and the vertical distance decreased, confirming the suppressed expansion of large pores. As shown in Figure 4(f), the T_2 range of the decreasing part of the T_2 spectrum for the mesopores was shorter after the test. This is because the fitting of particles reduced the seepage pores, which mostly are the macropores [24]. The expansion of the mesopores was insufficient to compensate for the compacted macropores, resulting in macropores approaching the size range of mesopores.

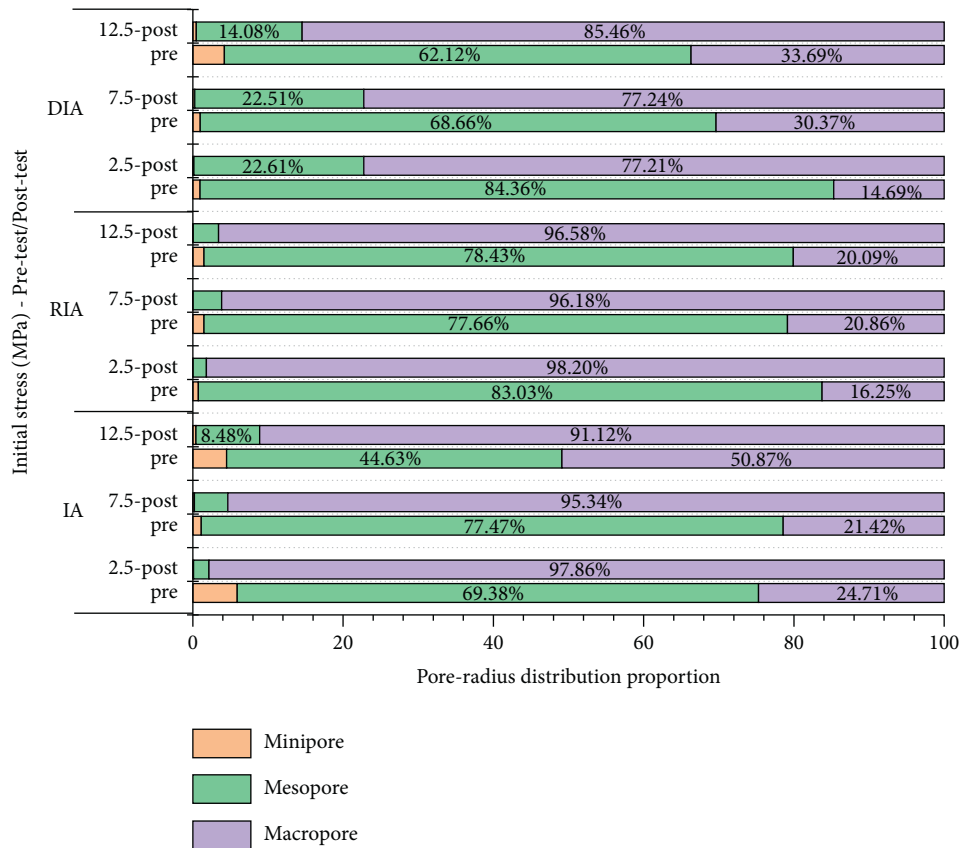
Furthermore, in this study, the pore-radius distributions for loading and unloading to σ_c and 80% of σ_c , respectively, were regarded as the pre- and posttest pore-radius distributions, respectively. According to the statistics for different pore radii, the distribution proportion of pores for each pore radius for the pre- and posttest limestone was obtained, as shown in Figure 5, and all the data are shown in Table 6.

As shown in Figure 5, with the exception of $\nu = 0.15$ mm/min, most of the rock samples exhibited the largest amount of mesopores before the test. The number of macropores was significantly larger before the test, and the proportion of minipores was generally reduced, indicating that loading and unloading caused minipores and mesopores inside the rock to penetrate a large number of macropores, and the increase in the pore radius reduced the overall aggregation force of the rock skeleton and particles [16], causing damage to the rocks.

As indicated by the IA cycling results in Table 6, with the increasing loading rate ν , the increase in the proportion of minipores from pretest to posttest changed from 1.1% to -5.82% and -3.72% , and the increase in the proportion of mesopores increased from 29.59% to -67.33% and -72.79% . The magnitude of the increase was reduced for the minipores and mesopores, whereas the proportion of macropores increased from -30.69% to 73.14% and 70.06%, representing a larger increase. The analysis indicates that a higher loading rate causes a larger plastic strain in the rocks (see Table 5) and higher viscoplasticity of the rock, promoting the pore expansion in the space generated by the plastic strain.



(a)



(b)

FIGURE 5: Pore-radius distribution proportion (a) at different loading rates and (b) at different initial peak stresses before and after the test.

TABLE 6: Pore-radius distribution proportion at different loading rates and initial peak stresses before and after the test.

Pore radius	Minipore (%)	Mesopore (%)	Macropore (%)	Pore radius	Minipore (%)	Mesopore (%)	Macropore (%)
	Pretest or posttest	Pre	Post	Pre	Post	Pre	Post
IA	As the loading rate ν increases	$\nu = 0.15$ mm/min	0.78	1.88	22.27	51.86	46.26
				$\Delta = 1.1$		$\Delta = 29.59$	$\Delta = -30.69$
		$\nu = 0.2$ mm/min	5.91	0.09	69.38	2.05	97.85
				$\Delta = -5.82$		$\Delta = -67.33$	$\Delta = 73.14$
		$\nu = 0.3$ mm/min	3.81	0.09	77.93	5.14	94.77
				$\Delta = -3.72$		$\Delta = -72.79$	$\Delta = 70.06$
	As the initial peak stress σ_0 increases	$\sigma_0 = 2.5$ MPa	5.91	0.09	69.38	2.05	97.85
				$\Delta = -5.82$		$\Delta = -67.33$	$\Delta = 73.14$
		$\sigma_0 = 7.5$ MPa	1.11	0.20	77.48	4.46	95.34
				$\Delta = -0.91$		$\Delta = -73.02$	$\Delta = 73.92$
		$\sigma_0 = 12.5$ MPa	4.50	0.40	44.63	8.48	91.12
				$\Delta = -0.15$		$\Delta = 16.64$	$\Delta = 82.61$
RIA	As the loading rate ν increases	$\nu = 0.15$ mm/min	10.31	0.75	75.38	16.64	82.61
				$\Delta = -9.56$		$\Delta = -58.74$	$\Delta = 68.30$
		$\nu = 0.2$ mm/min	0.72	0.02	83.03	1.78	98.21
				$\Delta = -0.70$		$\Delta = -81.25$	$\Delta = 81.96$
		$\nu = 0.3$ mm/min	7.30	0.05	92.70	5.93	94.02
				$\Delta = -7.25$		$\Delta = -86.77$	$\Delta = 94.02$
	As the initial peak stress σ_0 increases	$\sigma_0 = 2.5$ MPa	0.72	0.02	83.03	1.78	98.21
				$\Delta = -0.70$		$\Delta = -81.25$	$\Delta = 81.96$
		$\sigma_0 = 7.5$ MPa	1.48	0.03	77.66	3.79	96.17
				$\Delta = -1.45$		$\Delta = -73.87$	$\Delta = 75.31$
		$\sigma_0 = 12.5$ MPa	1.48	0.04	78.43	3.38	96.57
				$\Delta = -0.15$		$\Delta = 2.05$	$\Delta = 97.90$
DIA	As the loading rate ν increases	$\nu = 0.15$ mm/min	2.00	0.04	63.60	2.05	97.90
				$\Delta = -1.96$		$\Delta = -61.55$	$\Delta = 63.51$
		$\nu = 0.2$ mm/min	0.95	0.13	84.35	22.61	77.26
				$\Delta = -0.82$		$\Delta = -61.74$	$\Delta = 62.57$
		$\nu = 0.3$ mm/min	0.72	0.30	73.78	50.25	49.44
				$\Delta = -0.42$		$\Delta = -23.53$	$\Delta = 23.94$
	As the initial peak stress σ_0 increases	$\sigma_0 = 2.5$ MPa	0.95	0.13	84.35	22.61	77.26
				$\Delta = -0.82$		$\Delta = -61.74$	$\Delta = 62.57$
		$\sigma_0 = 7.5$ MPa	0.97	0.25	68.65	22.51	77.25
				$\Delta = -0.72$		$\Delta = -46.14$	$\Delta = 46.88$
		$\sigma_0 = 12.5$ MPa	4.19	0.46	62.12	14.08	85.46
				$\Delta = -3.73$		$\Delta = -48.04$	$\Delta = 51.77$

Therefore, faster loading intensifies the expansion of minipores and mesopores, resulting in the formation of macropores. With an increase in the initial peak stress σ_0 , the increase in the proportion of mesopores between pretest and posttest samples changed from -67.33% and -73.02% to -36.15% , and that for the macropores changed from 73.14% and 73.92% to 40.25% , i.e., the decrease in mesopores was small, and the increase in macropores was smaller. According to poromechanical theory, under a higher initial peak stress, more pore water is continuously discharged, which causes the compression of pores [26]. Consequently, the mesopores could not easily expand, resulting in small increases in mesopores and macropores.

As indicated by the RIA cycling results in Table 6, with an increase in the loading rate ν , the increase in the proportion of mesopores between pretest and posttest samples decreased from -58.74% to -86.77% , and the increase in the proportion of macropores increased from 68.30% to 94.02% . According to the analysis, a higher loading rate resulted in a

larger plastic strain and a greater degree of plastic fracture of the rocks (see Table 5), causing more expansions from mesopores to macropores. With an increase in the initial peak stress σ_0 , the increase in the proportion of mesopores increased from -81.25% to -75.05% , and the increase in the proportion of macropores decreased from 81.96% to 76.48% . According to the analysis, many complete loading processes were conducted in the RIA cycling, and the increase in the initial peak stress reduced the sensitivity of the pores; thus, pores were probably closed [25], reducing the expandability of the mesopores and hindering their expansion into macropores.

As indicated by the DIA cycling results in Table 6, with an increase in the loading rate ν , the increase in the proportion of minipores between pretest and posttest samples increased from -1.96% to -0.42% , and that for mesopores increased from -61.55% to -23.53% . However, that for the macropores decreased from 63.51% to 23.94% . According to the analysis, increasing the loading rate reduced the ab-

sorption energy of the rock [27], making it more difficult for the minipores and mesopores to expand significantly and form macropores. With an increase in the initial peak stress σ_0 , the increase in the proportion of mesopores increased from -61.74% to -48.04% , but the increase in the proportion of macropores decreased from 62.57% to 51.77% . According to the analysis, the disturbance cycles increased the loading time of the rock. The higher-stress disturbance cycles easily reclosed the pores opened during the previous unloading process, which enhanced the closure effect of the pores and hindered the expansion of mesopores into macropores [25]; however, the lower-stress disturbance cycle drove the rock to continue deforming and caused the pores to expand smoothly and steadily.

Summarizing the laws for the various loading and unloading methods, it can be concluded that the pore-radius enlargement and pore penetration degree under IA and RIA cycling are positively correlated with the loading rate but inversely correlated with the initial peak stress, respectively. Under DIA cycling, they are inversely correlated to both the loading rate and the initial peak stress. Combined with the changes in the plastic strain, it is clear that the variation laws of the pore radius with respect to the loading rate and the initial peak stress are identical to those of the plastic strain.

4.2. Changes in NMR T_2 Spectrum Distribution under Different Loading and Unloading Methods. Figure 6 shows the T_2 spectrum of rocks before and after the application of different loading and unloading methods. In the longitudinal direction, for IA cycling, the number of mesopores was increased after the test. The increase rate increased with the pore radius in the mesopores range, and the number of macropores increased significantly. The increase in macropores after the test under DIA cycling was small, and pores in certain ranges of mesopores radii decreased. The pore radius under the different loading and unloading methods increased in the following order: DIA < IA < RIA, which is consistent with the magnitude of the plastic strain under the different loading and unloading methods. According to the analysis, the number of complete loading and unloading cycles is an important factor that determines the degree of pore penetration and mesostructural damage. The damage caused by the disturbance cycle in DIA cycling reduced the number of complete loading and unloading cycles that the rock could experience; therefore, the pore-radius change was the smallest for DIA cycling. The most complete loading and unloading cycles occurred in RIA cycling, where the pores that did not reach the expansion limit in a loading section continued to expand in the constant peak stress cycle; therefore, the pore-radius changes and degree of mesostructural damage were the largest.

From a horizontal perspective, the T_2 value of the troughs for the mesopores and the peaks for the macropores after the test for DIA cycling were smaller than those of the other loading and unloading methods. According to analysis, the disturbance cycle in DIA cycling can promote not only the pore expansion but also the continuous outflow of water from the formed macropores, which enhances the

compressibility of the macropores, reducing the pore radius of the macropores during the loading and unloading and reducing the T_2 of the minipores and macropores after the test. Among the three loading and unloading methods, only after RIA cycling had the minipores increased significantly, indicating that the rocks were prone to newly formed minipores for a long time under RIA cycling, causing the accumulation of minipores due to the lack of expansion to mesopores.

4.3. Evolution of Porosity under Different Loading and Unloading Paths. The porosity can reflect the quantity of pores inside the rock. By studying its evolution law, the development process of mesoporous structure damage under various loading and unloading paths can be understood intuitively. Figure 7 shows the changes in porosity when limestone was loaded to stress levels of 0 and 20%, 40%, 60%, and 80% of σ_c under various loading and unloading methods. In general, before the loading to 40% of σ_c , the porosity decreased significantly with an increase in the loading stress level, which slowly decreased between 40% and 60% of σ_c and increased between 60% and 80% of σ_c . Three stages correspond to the compaction and linear-elastic stage, early part of the plastic stage, and late part of the plastic stage before the peak strength, respectively. Among them, the stress interval of the compaction and linear-elastic stage is the longest. This is because the pores were easily compacted during this period, and a large portion of the loading stress acting on the rock sample was consumed by the pore closure. Therefore, the times for compaction and linear elasticity were longer; in this process, water continuously filled and flowed out of the pores, promoting the compaction of the pores for a long time.

To analyze the change law of pore compaction and expansion, the porosity reduction from pretest to 60% of σ_c was defined as the pore compaction limit, and the porosity increase between pretest and 80% of σ_c was defined as the pore expansion limit.

As shown in Figure 7(a), under IA cycling, a higher initial porosity resulted in higher pore compaction and expansion limits. Under RIA cycling, the initial porosity of the rock was the lowest at the loading rate of $\nu = 0.15$ mm/min, and the pore compaction limit was the highest, indicating that the loading rate of $\nu = 0.15$ mm/min under RIA cycling promoted the compaction effect of the loading stress on the pores. The initial porosity at $\nu = 0.15$ mm/min was similar to that at $\nu = 0.2$ mm/min, but the pore expansion limit was significantly lower, indicating that the loading rate of $\nu = 0.15$ mm/min inhibited the pore expansion. Under DIA cycling, the rock porosity at $\nu = 0.3$ mm/min changed significantly between 0 and 40% of σ_c and changed less between 40% and 60% of σ_c , but the rock at $\nu = 0.15$ mm/min decreased uniformly between 0 and 60% of σ_c , although the initial porosity of which is the same as that at $\nu = 0.3$ mm/min. Moreover, its porosity compaction limit was lower than that at $\nu = 0.3$ mm/min. However, its porosity expansion limit was the highest among the three loading rates, indicating that the loading rate of $\nu = 0.15$ mm/min under DIA

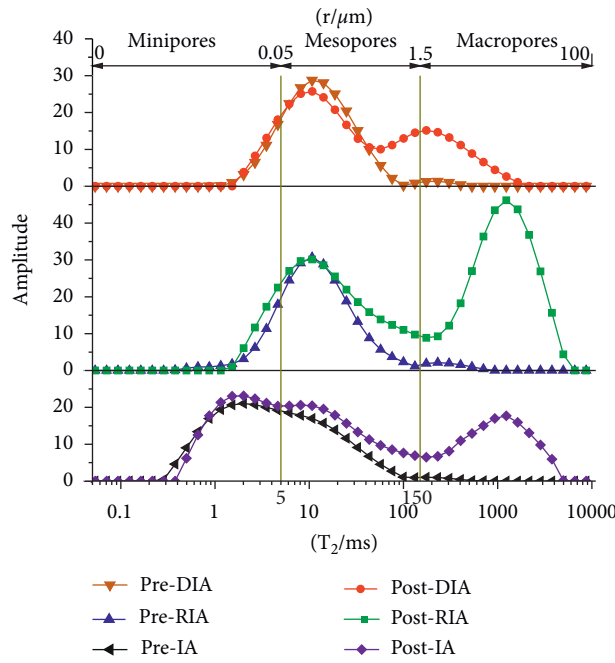


FIGURE 6: T_2 spectrum distribution under different loading and unloading methods ($v = 0.2 \text{ mm/min}$, $\sigma_0 = 2.5 \text{ MPa}$).

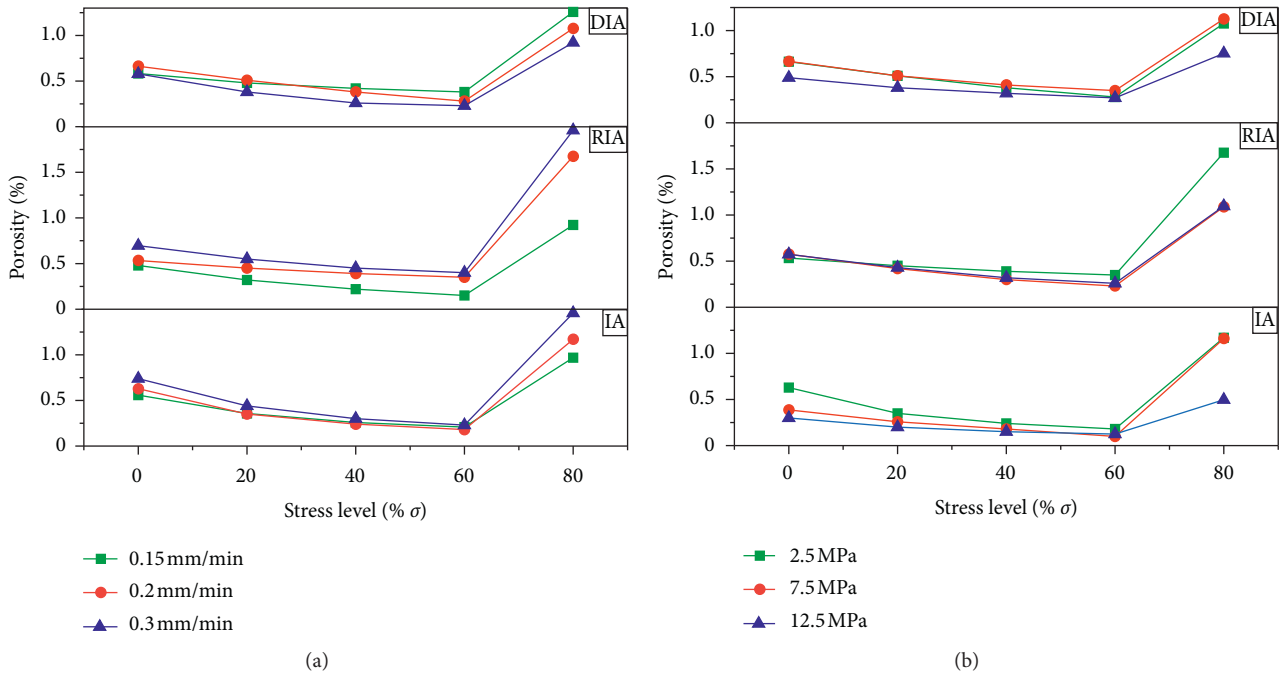


FIGURE 7: Porosity changes at different loading rates and initial peak stresses for each method: (a) different loading rates ($\sigma_0 = 2.5 \text{ MPa}$); (b) different initial peak stresses ($v = 0.2 \text{ mm/min}$).

cycling inhibited pore compaction and promoted pore expansion. The loading rate of $v = 0.3 \text{ mm/min}$ caused the time of the beginning of pore penetration in the plastic stage to advance from the late part of the plastic stage to the early part, making the compaction behavior of the pores in the early plastic stage less prominent, which allowed for rapid expansion of the pores.

As shown in Figure 7(b), in the case of IA cycling, a higher initial porosity resulted in higher pore compaction

and expansion limits. However, when the initial porosity of the rock at the initial peak stress of $\sigma_0 = 2.5 \text{ MPa}$ was higher than that at $\sigma_0 = 7.5 \text{ MPa}$, the pore expansion limit was lower in the former case, indicating that $\sigma_0 = 2.5 \text{ MPa}$ under IA cycling inhibited the development and expansion of pores. Under RIA cycling, the initial porosities of the rock sample were identical at $\sigma_0 = 2.5$ and 7.5 MPa , but the pore compaction and expansion limits were lower in the former case. This indicates that, under RIA cycling, loading and

unloading with $\sigma_0 = 2.5$ MPa reduced the amount of compressible pores and simultaneously promoted deeper expansion and penetration of pores. Under DIA cycling, the initial porosities of the rock sample were identical for $\sigma_0 = 2.5$ and 7.5 MPa. However, the pore compaction limit was higher in the former case, indicating that, for DIA cycling, reducing the initial peak stress can enhance the compressibility of the pores.

5. Discussion

As the degree of compression of the rock increases gradually in the loading and unloading, the pore water in the macropores within the rock is continuously transferred to the expanding minipores and causes the compression of the minipores. Protons exhibit signals, and H protons are only present in the water in the pores. Therefore, the evolutionary characteristics of the pore water can directly reflect the evolutionary characteristics of the mesostructural damage of the rock.

Pore water includes bound and free water. When the pore diameter is the lower threshold value, the capillary pressure constraint prevents the water in the pores from flowing. This pore-diameter threshold value corresponds to a T_2 time threshold, which is the $T_{2 \text{ cutoff}}$ value. The flow of free water between pores is more active, and the bound water appears calmer because it is tightly enclosed in the pores. Therefore, the pores generated by free water are more likely to cause deformation and damage [28].

According to the carbonate rock test results of Straley [29], the pretest $T_{2 \text{ cutoff}}$ value of rocks was 100 ms. Minipores hardly affect the promotion of pore-water flow [30]. Therefore, in the present study, the peak of the mesopores was considered as the first peak, and that of the macropores was considered as the second peak. The pretest T_2 spectrum of each rock sample in Figure 4 indicates that the first peak amplitude (hereinafter referred to as A1) was greater than the second peak amplitude (hereinafter referred to as A2); however, two types of morphological features of A1 < A2 (Figure 4(e)) and A1 > A2 (Figure 4(f)) were observed after the test. In each case, one rock sample each at $\nu = 0.2$ mm/min and $\sigma_0 = 2.5$ MPa (the sample numbers were L22 and L32, respectively) were used to analyze the $T_{2 \text{ cutoff}}$ value and pore-water evolution characteristics after the test.

As shown in Figure 4(e), the L22 rock sample after the test at $\nu = 0.2$ mm/min and $\sigma_0 = 2.5$ MPa belonged to the A1 < A2 type, and its $T_{2 \text{ cutoff}}$ value was the T_2 corresponding to the median value of the first peak and the later valley [31]. As shown in Figure 4(e), this value was 57.22 ms.

As shown in Figure 4(f), the L32 rock sample after the test at $\nu = 0.2$ mm/min and $\sigma_0 = 2.5$ MPa did not satisfy the condition of A1 < A2. Its $T_{2 \text{ cutoff}}$ value was calculated using the fitting experience formula as follows [31]:

$$T_{2 \text{ cutoff}} = 1.1732(T_2 LM)^{0.8573}, \quad (6)$$

where $T_2 LM$ represents the geometric mean of T_2 .

Using equation (5), the posttest $T_{2 \text{ cutoff}}$ value of the L32 rock sample was calculated as $1.1732 \times (79.9757)^{0.8573} = 50.21$ ms. In summary, the pretest $T_{2 \text{ cutoff}}$ value of the rock sample was 100 ms. The posttest $T_{2 \text{ cutoff}}$ value of A1 < A2-type rock samples was 57.22 ms, and that of A1 > A2-type rock samples was 50.21 ms.

The aforementioned $T_{2 \text{ cutoff}}$ value and the corresponding amounts of pores in the bound-water and free-water SEM images are presented in Figure 8. Owing to the similarity of the pore size, only the pore structure of the pretest L32 rock sample is shown. Clearly, bound water primarily existed in the pores of the organic matter [32] and in mesopores with radii ranging from 1 to 1.5 μm , indicating that these pores had a relatively weak driving effect on water-molecule migration. Free water primarily existed in the macropores, indicating that the migration behavior of water molecules primarily depended on the macropores [33]. Before the test, the macropores primarily comprised pores with radii of $>10 \mu\text{m}$ that formed along the intragranular fracture. However, after the test, they primarily comprised transgranular fractures, indicating that the damage force of the loading and unloading was relatively large, which led to a high probability of transgranular fracture.

According to the T_2 range dividing bound water and free water, the pretest and posttest proportions of bound water and free water for the rocks under different loading and unloading paths were calculated. The results are presented in Table 7. Clearly, after the test, the bound-water content in the rock pores was reduced, but the free-water content was increased. This indicates that the loading and unloading enhanced the flowability of the pore water in the saturated limestone, increasing the amount of free water. Additionally, the flow of free water through the pores weakened the ability of the pores to resist the squeeze force between particles, causing the pores to expand easily and hence damage the rock. Because the bound water had significantly more pores than the free water before the test, the weak migration behavior of the water molecules was not conducive to the pore-water pressure enhancing the pore connectivity, resulting in slower development of the mesostructural damage to the rocks during the early loading and unloading.

As shown in Table 7, the evolution characteristics of the pore water under different loading and unloading paths differed. At the same loading rate of 0.2 mm/min, the reduction in bound water decreased with an increase in the initial peak stress σ_0 . At the same initial peak stress of 2.5 MPa, the reduction in bound water under DIA cycling decreased gradually with an increase in the loading rate ν , but the reduction in bound water under IA and RIA cycling increased with the loading rate. The change law for the bound-water reduction with respect to the loading rate and initial peak stress under each loading and unloading method was consistent with that for the plastic strain. Analyses revealed that a larger reduction in the amount of bound

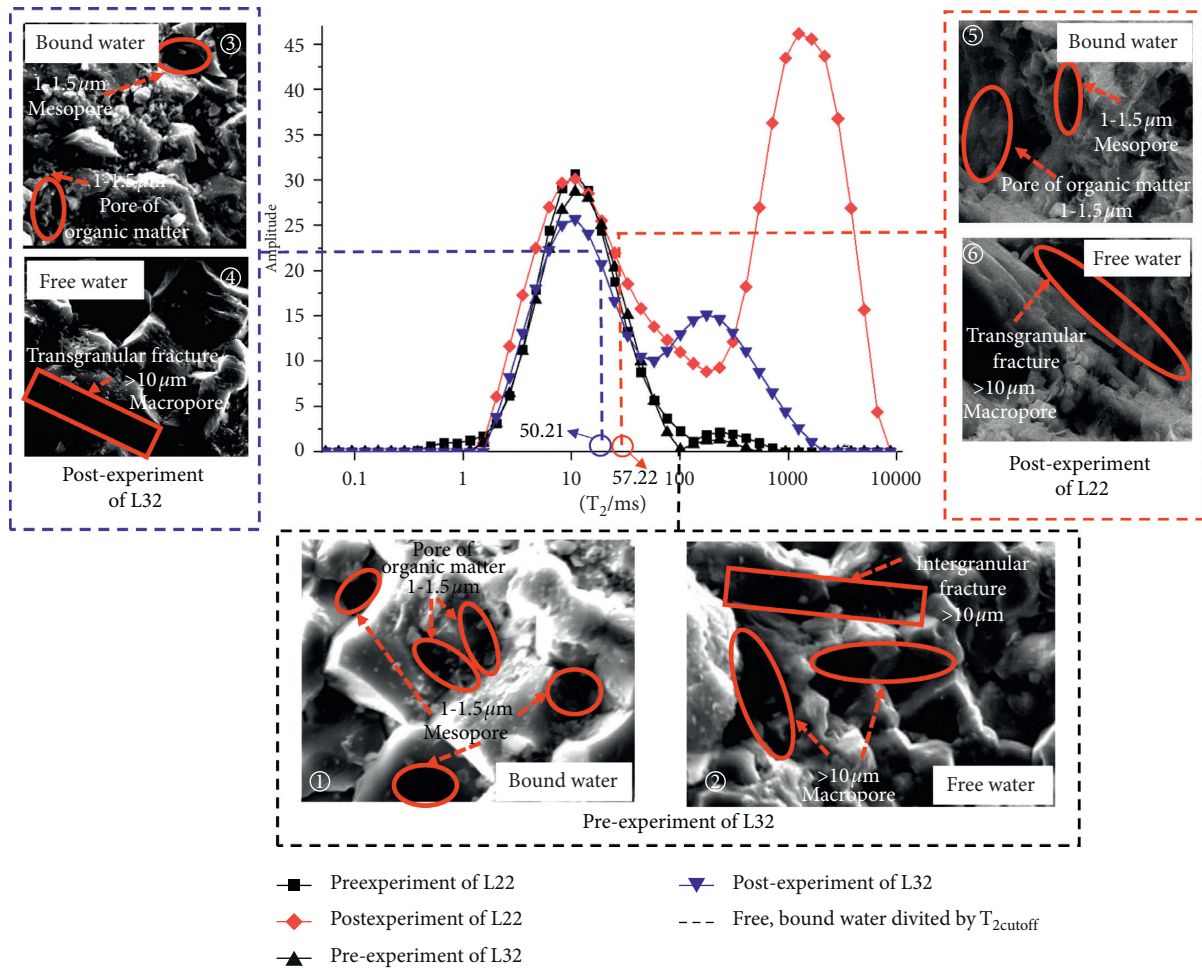


FIGURE 8: Mesopore structure of bound water and free water in L22 and L32 rock samples. ③ and ⑤ show the pore structure of bound water in the two rock samples after the test. ④ and ⑥ show the free-water pore structures after the test. ① and ② show the bound-water and free-water pore structures before the test.

TABLE 7: Distributions of bound water and free water before and after loading and unloading.

Loading and unloading path	Pretest or posttest	Pore proportions for IA			Pore proportions for RIA			Pore proportions for DIA			
		Bound water/%	Free water/%	Bound-water reduction/%	Bound water/%	Free water/%	Bound-water reduction/%	Bound water/%	Free water/%	Bound-water reduction/%	
At $\sigma_0 = 2.5$ MPa, as the loading rate ν increases	$\nu = 0.15$ mm/min	Pre	94.67	5.33	1.53	99.39	0.61	22.79	97.23	2.77	46.40
		Post	93.14	6.86		76.60	23.40		50.83	49.17	
	$\nu = 0.2$ mm/min	Pre	99.79	0.21	25.56	97.76	2.24	52.61	97.87	2.13	33.38
		Post	74.23	25.77		45.15	54.85		64.49	35.51	
	$\nu = 0.3$ mm/min	Pre	95.93	4.07	36.03	95.86	4.14	53.18	96.50	3.50	2.28
		Post	59.90	40.10		42.68	57.32		94.22	5.78	
At $\nu = 0.2$ mm/min, as the initial peak stress σ_0 increases	$\sigma_0 = 2.5$ MPa	Pre	99.79	0.21	25.56	97.76	2.24	52.61	97.87	2.13	33.38
		Post	74.23	25.77		45.15	54.85		64.49	35.51	
	$\sigma_0 = 7.5$ MPa	Pre	95.93	4.07	24.93	99.01	0.99	52.15	96.94	3.06	30.83
		Post	71.00	29.00		46.86	53.14		66.11	33.89	
	$\sigma_0 = 12.5$ MPa	Pre	98.14	1.86	0.84	97.48	2.52	51.79	96.83	3.17	18.54
		Post	97.30	2.70		45.69	54.31		78.29	21.71	
Average reduction of bound water				17.78			46.50			26.49	

water resulted in more pores containing water with a strong percolation capacity, and in the process of continuous water percolation, the pore-water pressure and axial loading stress transmitted to the pore surface had a greater repeated extrusion effect on the pores. This increased the fatigue and softening of the pores, making them easier to expand, and created a larger space for relative sliding of particles, increasing the plastic strain on the rock during loading and unloading.

The average bound-water reduction under the different loading and unloading methods in Table 7 decreased in the following order: RIA > DIA > IA. It is considered that the constant peak stress cycle after the loading section allowed water molecules that had not migrated sufficiently in the loading section to continue to migrate, thereby increasing the amount of free water and reducing the amount of bound water. Additionally, it can be considered that the stress amplitude of the constant peak stress cycle determined the activity of the water molecules in the pores. The stress amplitude of the disturbance cycle was small in DIA cycling; therefore, the bound-water reduction was smaller than that in RIA cycling.

6. Conclusions

- (1) When loading and unloading progressed from 0 to 40% of σ_c , with the increasing stress, the porosity decreased rapidly, which decreased slowly from 40% to -60% of σ_c , and increased rapidly from 60% to 80% of σ_c . Under IA cycling, a higher initial porosity resulted in higher pore compaction and expansion limits, reducing the initial peak stress inhibited pore expansion. Under RIA cycling, reducing the loading rate promoted pore compaction and suppressed the expansion of pores, and reducing the initial peak stress suppressed pore compaction. The opposite trends were observed for DIA cycling. The evolution of the porosity was accurately described by a third-order polynomial model.
- (2) As the initial peak stress increased, the plastic strain of the rock decreased gradually, and the residual stress and strength increased accordingly. With an increase in the loading rate, the plastic strain increased gradually, and the residual stress decreased gradually under IA and RIA cycling, whereas the opposite trends were observed under DIA cycling. The durability of the rock against external forces under different loading and unloading methods was directly proportional to the total duration of the complete loading and unloading processes.
- (3) As the initial peak stress increased, the pore-radius distribution changed, and the reduction in the amount of bound water decreased gradually. With the increase in the loading rate, the mesostructure parameters under IA and RIA cycling increased gradually; however, they decreased under DIA cycling. The loading rate of 0.2 mm/min promoted the expansion of minipores and mesopores under RIA cycling.
- (4) The loading and unloading reduced the bound-water content in the pores and increased the free-water content, which damaged the rocks by softening the pores, causing them to experience fatigue. The reduction in the amount of bound water for the different loading and unloading methods decreased in the following order: RIA > DIA > IA.

Data Availability

This study was supported by multiple datasets, which are openly available at locations cited in the reference section.

Conflicts of Interest

The authors declare that there are no conflicts of interest regarding the publication of this paper.

Acknowledgments

This work was supported in part by the Key Laboratory of Rock Mechanics and Geohazards of Zhejiang Province (grant no. ZJRMG-2018-Z03); the National Natural Science Foundation of China (grant no. 51774323); Hunan Provincial Natural Science Foundation of China (grant no. 2020JJ4712); and the Fundamental Research Funds for the Central Universities of Central South University (grant no. 2019zzts671).

References

- [1] Y.-H. Huang, S.-Q. Yang, and W. Zeng, "Experimental and numerical study on loading rate effects of rock-like material specimens containing two unparallel fissures," *Journal of Central South University*, vol. 23, no. 6, pp. 1474–1485, 2016.
- [2] H. Q. Shuang, S. G. Li, L. Liu, G. F. Chen, and K. I. Song, "Use of acoustic emission for the detection of brittle rock failure under various loading rates," *Advance in Civil Engineering*, vol. 2018, 2018.
- [3] A. Taheri, N. Yfantidis, C. Olivares, B. Connelly, and T. Bastian, "Experimental study on degradation of mechanical properties of sandstone under different cyclic loadings," *Geotechnical Testing Journal*, vol. 39, no. 4, pp. 673–687, 2016.
- [4] L. Weng, Z. J. Wu, and Q. S. Liu, "Evaluating damage and microcracking behavior of granite using NMR testing under different levels of unconfined compression," *International Journal of Geomechanics*, vol. 19, no. 1, 2018.
- [5] Z. J. Wu, W. J. Cui, L. F. Fan, and Q. S. Liu, "Mesomechanism of the dynamic tensile fracture and fragmentation behaviour of concrete with heterogeneous mesostructure," *Construction and Building Materials*, vol. 217, pp. 573–591, 2019.
- [6] K. P. Zhou, S. H. Su, Z. X. Hu, J. L. Li, and Z. Yang, "Experimental research into nuclear magnetic resonance in marble with different initial damages under unloading conditions," *So Rock and Soil Mechanics*, vol. 36, no. 8, pp. 2144–2150, 2018.
- [7] P. Phukon, A. Y. Sen, K. Sen, and H. B. Srivastava, "Variation in mechanism of dynamic recrystallization and differential stress across the Chiplakot Crystalline Belt, Kali River Valley, Kumaun Himalaya: implications for exhumation of basement rocks in a "critical taper wedge" setting," *Himalayan Geology*, vol. 40, no. 2, pp. 169–181, 2019.

- [8] S. Rahal, A. Sellier, and G. Casaux-Ginestet, "Poromechanical consolidation and basic creep interactions around tunnel excavation," *International Journal of Rock Mechanics and Mining Sciences*, vol. 94, pp. 55–63, Apr. 2017.
- [9] ISRM B E, "Basic geotechnical description of rock masses," *International Journal of Rock Mechanical Mine Science Geomechanical Abstracts*, vol. 18, pp. 85–110, 1981.
- [10] J. Li, L. Hong, K. Zhou, C. Xia, and L. Zhu, "Influence of loading rate on the energy evolution characteristics of rocks under cyclic loading and unloading," *Energies*, vol. 13, no. 15, p. 4003, 2020.
- [11] M. G. Qian, P. W. Shi, and J. L. Xu, *Ground Pressure and Strata Control*, China University of mining and technology Press, Xuzhou, China, 2010.
- [12] J. Dai, X. J. Liu, and X. J. Liu, "The change regularity of abutment pressure under various propulsive distance in coal face," *Advanced Materials Research*, vol. 524-527, p. 769, 2012.
- [13] F. Cui, S. Dong, X. P. Lai, J. Q. Chen, J. T. Cao, and P. F. Shan, "Study on rule of overburden failure and rock burst hazard under repeated mining in fully mechanized top-coal caving face with hard roof," *Energies*, vol. 12, no. 24, 2019.
- [14] D. N. Shurygin, V. M. Kalinchenko, V. A. Tkachev, and A. Y. Tretyak, "Mathematical methods in geometrization of coal field," *Innovations And Prospects Of Development Of Mining Machinery And Electrical Engineering*, vol. 87, 2017.
- [15] T. Chen, Q.-I. Yao, F. Wei et al., "Effects of water intrusion and loading rate on mechanical properties of and crack propagation in coal-rock combinations," *Journal of Central South University*, vol. 24, no. 2, pp. 423–431, 2017.
- [16] J. Li, R. B. Kaunda, and K. Zhou, "Experimental investigations on the effects of ambient freeze-thaw cycling on dynamic properties and rock pore structure deterioration of sandstone," *Cold Regions Science And Technology*, vol. 154, pp. 133–141, 2018.
- [17] R. Ausbrooks, N. F. Hurley, A. May, and D. G. Neese, *Pore-size Distribution in Vuggy Carbonates from Core Images, NMR, and Capillary Pressure*, SPE Annual Technical Conference and Exhibition, Houston, TX, USA, 1999.
- [18] A. Matteson, J. P. Tomanic, M. M. Herron, D. F. Allen, and W. E. Kenyon, "NMR relaxation of clay/brine mixtures," *SPE Reservoir Evaluation & Engineering*, vol. 3, no. 05, pp. 408–413, 2000.
- [19] Y. Li and J. Li, "Experimental NMR T2 distribution properties of tight carbonate reservoir, Da'anzhai Formation, Sichuan Basin, Southwest China," in *Proceedings of the 2016 Workshop: Rock Physics and Borehole Geophysics*, Beijing, China, August 2016.
- [20] L. J. Ma, B. Peng, and Q. C. Yu, "Porosity and permeability characteristics of Carboniferous dense limestone in the east of Qaidam Basin," *Carsologica Sinica*, vol. 36, no. 1, pp. 15–22, 2017.
- [21] J. W. Jiang and X. Xu, "Evaluation and productivity prediction of complex carbonate reservoir in H oilfield of Middle East," *Journal of Southwest Petroleum University (Science & Technology Edition)*, vol. 38, no. 5, pp. 33–40, 2016.
- [22] L. Yan, L. S. Liu, S. H. Zhang, D. P. Lan, and J. C. Liu, "Testing of weakly weathered granites of different porosities using a split hopkinson pressure bar technique," *Advances in Civil Engineering*, vol. 2018, 2018.
- [23] Q. Xiao, X. Zhao, W. Lin, X. Huang, and Z. Song, "Application of NMR to test sandstone stress sensitivity of the dongfang X gas field, China," *Institute of Electrical and Electronics Engineers Access*, vol. 7, pp. 95212–95223, 2019.
- [24] Z. Liu, W. Y. Wang, H. Yang, S. J. Yu, and L. Xin, "Experimental study on the fractal pattern of a coal body pore structure around a water injection bore," *Journal of Energy Resources Technology-Transactions of the ASME*, vol. 142, no. 1, 2020.
- [25] H. L. Wang, W. Y. Xu, M. Cai, Z. P. Xiang, and Q. Kong, "Gas permeability and porosity evolution of a porous sandstone under repeated loading and unloading conditions," *Rock Mechanics and Rock Engineering*, vol. 50, no. 8, pp. 2071–2083, 2017.
- [26] C. L. Zhong, Y. Chunlin, Z. Y. Zhang, P. G. Ranjith, Y. Lu, and X. Choi, "The role of pore water plays in coal under uniaxial cyclic loading," *Engineering Geology*, vol. 257, 2019.
- [27] E. Kim, A. Garci, and H. Changani, "Fragmentation and energy absorption characteristics of Red, Berea and Buff sandstones based on different loading rates and water contents," *Geomechanics and Engineering*, vol. 14, no. 2, pp. 151–159, 2018.
- [28] M. L. Boyce and K. Gawankar, "Sequential fluid characterization: a new method using high-field-core nuclear magnetic resonance to characterize source-rock porosity and fluids," *SPE Reservoir Evaluation & Engineering*, vol. 22, no. 02, pp. 428–440, May. 2019.
- [29] C. Straley, D. Rossini, H. J. Vinegar, and H. J. Vinegar, "Core analysis by low-field NMR," *Log Analysts*, vol. 38, no. 2, pp. 84–93, 1997.
- [30] N. Brantut, M. Baker, L. N. Hansen, and P. Boud, "Microstructural control of physical properties during deformation of porous limestone," *Journal of Geophysical Research-Solid Earth*, vol. 123, no. 6, pp. 4751–4764, 2019.
- [31] C. L. Zhang, *Study of NMR Core Experiment Variable T2 Cutoff Value and Application Study of Reservoir Assessment*, Yangtze University, Jingzhou, China, 2016.
- [32] R. G. Loucks, R. M. Reed, S. C. Ruppel, and U. Hammes, "Spectrum of pore types and networks in mud rocks and a descriptive classification for matrix-related mudrock pores," *AAPG Bulletin*, vol. 96, no. 6, pp. 1071–1098, 2012.
- [33] R. P. Chen, S. Qi, H. L. Wang, and Y. J. Cui, "Microstructure and hydraulic properties of coarse-grained subgrade soil used in high-speed railway at various compaction degrees," *Journal of Materials in Civil Engineering*, vol. 31, no. 12, 2019.